

1 **Reconciling the long-term growth of the Northeastern Tibetan Plateau and the**
2 **upstream Yellow River profile**

3
4 X. He¹, X. P. Yuan^{1*}, C. Q. He², X. Y. Wang³, and X. M. Shen⁴

5
6 ¹Hubei Key Laboratory of Critical Zone Evolution, School of Earth Sciences, China University of
7 Geosciences, Wuhan, China.

8 ²Department of Earth, Atmospheric and Planetary Science, Massachusetts Institute of Technology,
9 Cambridge, USA.

10 ³School of Geography and Ocean Science, Nanjing University, Nanjing, China.

11 ⁴National Institute of Natural Hazards, Ministry of Emergency Management of China, Beijing, China

12
13 *Corresponding author: Xiaoping Yuan (yuanxiaoping@cug.edu.cn)

14
15 **Key Points:**

- 16 • The long-term growth of the Northeastern Tibetan Plateau is investigated by a landscape
17 evolution model with two growth scenarios.
- 18 • The Northeastern Tibetan Plateau experienced an early block uplift (~20-12 Ma) and a late
19 outward propagation uplift (~12-0 Ma).
- 20 • Our model results reconcile the long-term growth of the Northeastern Tibetan Plateau and the
21 upstream Yellow River profile.
- 22

23 Abstract

24 The growth history of the Northeastern Tibetan Plateau (NETP) is enigmatic, with debates on
25 when and how the NETP significantly uplifted. Here, we use a numerical landscape evolution
26 model to quantitatively investigate the ~20 Ma growth history of the NETP by studying the
27 formation history of the upstream Yellow River (UYR). Compared to the observed river profiles,
28 erosion rates, the trend of acceleration time of deformation, and paleo-elevation, our modeling
29 results suggest that the long-term growth history of the NETP consists of an early block uplift
30 (~20-12 Ma) and a late outward propagation uplift (~12-0 Ma). Before ~12 Ma (middle Miocene),
31 the NETP was uplifted via a block growth, with major uplift in the south part. Subsequently, the
32 high (~5 km) NETP has been uplifted via a northward propagation growth until the present-day
33 time. We further suggest that pure headward erosion unlikely formed the observed river profile of
34 the UYR over the past few million years. Our modeling thus reconciles the long-term outward
35 growth of the NETP and the UYR profile, suggesting a downstream migration of high erosion
36 rates, which is fundamentally different from the headward erosion of small mountain rivers. The
37 downstream propagation of fluvial erosion may commonly occur in the outward-growing plateau
38 on Earth.

39

40 Plain Language Summary

41 Mountain rivers with their river profiles can record the long-term growth history of orogen. The
42 Yellow River, the sixth longest river in the world, flows through the Northeastern Tibetan Plateau.
43 The upstream Yellow River profile provides an opportunity to quantitatively investigate the
44 controversial growth history of the Northeastern Tibetan Plateau. We study the formation history
45 of the Northeastern Tibetan Plateau by a numerical landscape evolution model combining with
46 two possible growth scenarios. Reconciling the long-term growth of the Northeastern Tibetan
47 Plateau and the upstream Yellow River profile, our modeled results show that the Northeastern
48 Tibetan Plateau experienced an early block uplift (~20-12 Ma) and a late outward propagation
49 uplift (~12-0 Ma). Furthermore, the observed upstream Yellow River profile is unlikely formed
50 by pure headward erosion over the past few million years indicated by previous studies. This work
51 further suggests that the downstream migration pattern of high erosion rates commonly exists in
52 tectonically active outward-growing plateaus on Earth.

53 1 Introduction

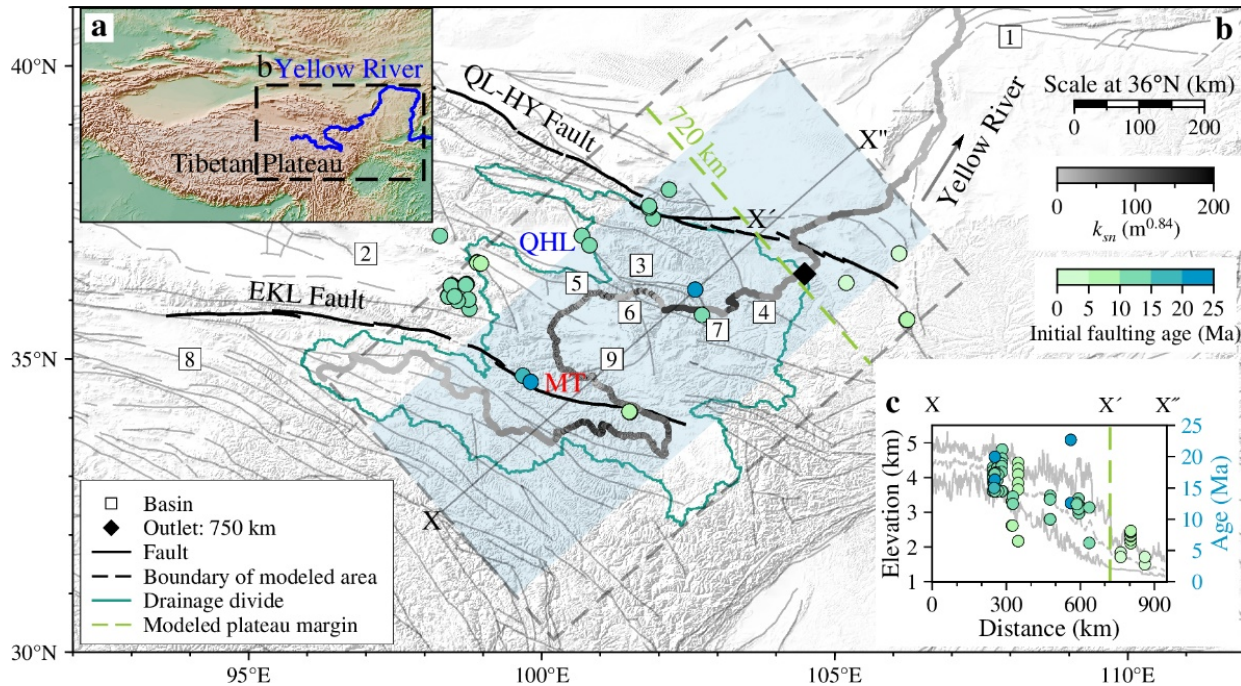
54 The Indian-Eurasian continent-continent collision (since ~55 Ma) controls the long-term
55 growth history of the Tibetan Plateau (Yin and Harrison, 2000), influencing Asian climate change
56 (An et al., 2001; Kutzbach et al., 1993), landscape evolution in Asia (Law and Allen, 2020; Shen
57 et al., 2022; Yuan et al., 2021), biodiversity (Klaus et al., 2016), and carbon cycle (Guo et al.,
58 2021; Märki et al., 2021). The critical evidence for the above research is related to when and how
59 the Tibetan Plateau grew. However, the timing of reaching the present-day high elevations (Fang
60 et al., 2020; Rowley and Currie, 2006; Su et al., 2019) and the mechanism of the plateau growth
61 (Clark and Royden, 2000; England and Houseman, 1989; Royden et al., 1997; Tapponnier et al.,
62 2001) remain highly debated.

63 With the growth of the Tibetan Plateau, the growth history of the NETP is still in dispute.
64 Some researchers suggest that the Indian-Eurasian collision (since ~55 Ma) influenced the NETP
65 soon after the collision (Clark et al., 2010; Dupont-Nivet et al., 2004), but the influences are
66 thought to be only an immediate response to the far-field effect of collision (Dayem et al., 2009).
67 Significant tectonic deformation and uplift of the NETP did not occur long time after the collision
68 (Dai et al., 2006; Wang et al., 2017, 2022). For example, various sediment accumulation rates
69 indicate that the Xining basin (Figure 1b) initiated at 55-52.5 Ma, but most tectonic activities
70 occurred after 17 Ma (Dai et al., 2006). In the Qaidam Basin (Figure 1b), Cenozoic sediments
71 initiated at ~25.5 Ma based on magnetostratigraphy and mammalian biostratigraphy (Wang et al.,
72 2017), and ~30 Ma based on magnetostratigraphies combined with detrital apatite fission-track
73 ages (Wang et al., 2022). Moreover, the initially significant activity ages in the NETP were near
74 the Miocene (~23-5.3 Ma) (Duvall et al., 2013; Lease et al., 2011; Li et al., 2019, 2022; Yuan et
75 al., 2011; Zhang et al., 1991; Zheng et al., 2006), and became younger to the northeast (Figure 1b,
76 c). Additionally, how the NETP uplifted is still unclear, with contrasting views including the
77 stepwise block extrusion and uplift to the north (Tapponnier et al., 2001) and the progressive
78 propagation uplift to the north via the lower crustal flow (Clark and Royden, 2000).

79 Mountain rivers form along with the growth of orogens, thus the longitudinal river profiles
80 can record the long-term orogenic growth history (Allen, 2008; Goren et al., 2014; Kirby et al.,
81 2003; Pritchard et al., 2009; Whipple and Tucker, 1999). Examples include the southeastern
82 Tibetan Plateau (Yuan et al., 2022), the Andes Orogen (Fox et al., 2015), the Anatolian Plateau
83 (Racano et al., 2021), and the Colorado Plateau (Roberts et al., 2012). The Yellow River, the sixth

84 longest river in the world, flows through the NETP (Figure 1), and the UYR likely recorded the
 85 long-term growth history of the NETP. Although there are still some debates on the formation time
 86 (Craddock et al., 2010; Lin et al., 2001) and the formation process (Craddock et al., 2010; Lin et
 87 al., 2001) of the UYR, its longitudinal profile offers an opportunity to reconstruct the NETP growth
 88 history by reproducing the UYR river profile.

89



90 **Figure 1.** Geological and topographical background of the study area. (a) Topography of the Tibetan Plateau.
 91 (b) Closer view of the study area with the Yellow River in the Northeastern Tibetan Plateau. The trunk of
 92 the Yellow River is colored with the channel steepness $k_{sn} = SA^{m/n}$ with $m/n = 0.42$ (Harkins et al., 2007).
 93 QL-HY Fault: Qilian-Haiyuan Fault; EKL Fault: East Kunlun Fault; QHL: Qinghai Lake; MT: Anyemaqen
 94 Shan. Basins (square with black frames) are in (b): (1) Hetao Basin, (2) Qaidam Basin, (3) Xining Basin,
 95 (4) Lanzhou Basin, (5) Gonghe Basin, (6) Guide Basin, (7) Linxia Basin, (8) Hoh Xil Basin, and (9) Zeku
 96 Basin. The initially significant activity ages (Table S1) are from references (Duvall et al., 2013; Lease et
 97 al., 2011; Li et al., 2019, 2022; Yuan et al., 2011; Zhang et al., 1991; Zheng et al., 2006). (c) The swath
 98 profile plots (maximum, average, and minimum elevations) are based on the blue shading area in (b) with
 99 initially significant activity ages. The modeled area is $950 \times 600 \text{ km}^2$. The width of the swath profile is 400
 100 km. The green dashed line at 720 km indicates the plateau margin. The black arrow shows the direction of
 101 river flow.

103

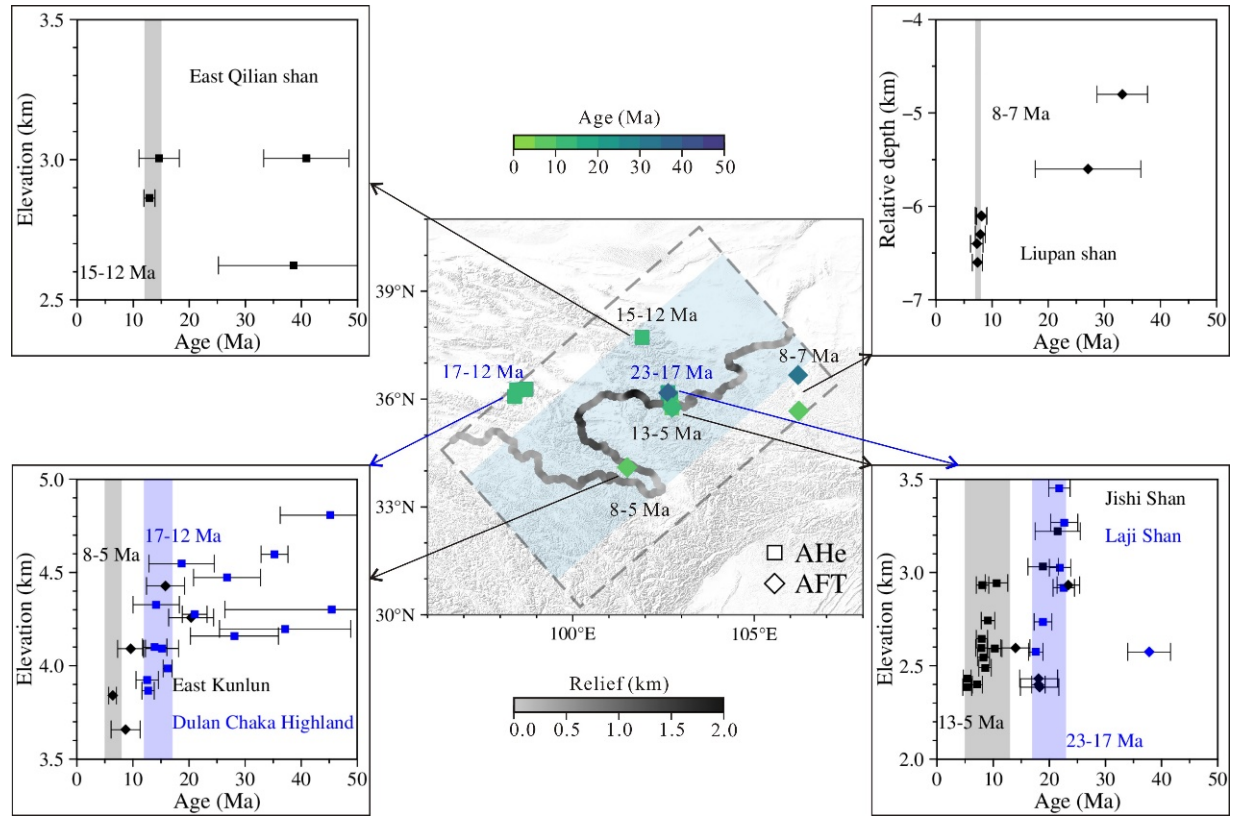


Figure 2. Thermochronometric ages and age-elevation relationships in the Northeastern Tibetan Plateau. AHe: Apatite (U-Th)/He; AFT: Apatite Fission Track. Thermochronometric ages (Table S2) are from references (Duvall et al., 2013; Lease et al., 2011; Wang et al., 2020; Zheng et al., 2006). The relief is calculated based on the difference between maximum and minimum elevations in the blue shading area.

This work aims to quantitatively study the ~20 Ma NETP growth history and the UYR formation history based on a numerical landscape evolution model (FastScape) (Braun and Willett, 2013; Yuan et al., 2019). In the NETP, we collected geomorphic data (e.g., river profile, swath profile, and relief), erosion rates, and the trend of acceleration times of deformation (e.g., initially significant activity ages and thermochronometric age-elevation relationships; Figures 1c and 2). In section 2, we propose two potential growth scenarios for the NETP growth, and then modify the numerical model to combine with two growth scenarios and several free parameters. In section 3, we test 2352 simulations with three free parameters to extract the modeled river profiles of each model. Based on the match of the observed and modeled river profiles, we obtain one of the best-fit modeled results in each growth model. Section 4 shows the NETP growth model by comparing the observed and modeled results, including the longitudinal river profiles, swath profiles, erosion

121 rates, and the trend of acceleration times of deformation (e.g., initially significant activity ages and
 122 thermochronometric age-elevation relationships). Based on the modeled and observed results, we
 123 discuss the NETP growth history together with the UYR formation history. Furthermore, we test
 124 our results against a possibly formed UYR with a retreat process and period of pure headward
 125 erosion.

126

127 **2. Methods**

128 **2.1 Landscape evolution model**

129 The landscape evolution model FastScape (Braun and Willett, 2013; Yuan et al., 2019) is
 130 used to simulate the uplift, fluvial erosion, and sediment transport and deposition processes in the
 131 drainage basin of the UYR as

$$132 \frac{\partial h}{\partial t} = U - K_f \tilde{p}^m A^m S^n + \frac{G}{\tilde{p} A} \int_A \left(U - \frac{\partial h}{\partial t} \right) dA, \quad (1)$$

133 where h is the elevation, t is the time, U is the tectonic uplift rate, K_f is the erodibility, A is the
 134 drainage area, S is the local slope in the steepest-descent direction of water flow, m is the area
 135 exponent, and n is the slope exponent. Dimensionless \tilde{p} represents any spatial or temporal
 136 variation in precipitation relative to the mean precipitation rate. Dimensionless G scales the
 137 deposition coefficient. To simplify the model, the dimensionless \tilde{p} is assumed uniform ($\tilde{p} = 1$),
 138 and the dimensionless G is assumed uniform ($G = 1$; Guerit et al., 2019; Yuan et al., 2019). We
 139 use the slope exponent $n = 1$ and $m = 0.42$ (i.e., $m/n = 0.42$) based on previous studies (e.g.,
 140 Harkins et al., 2007). Although Harkins et al. (2007) suggest the slope exponent n is less than
 141 unity, for values of $n \neq 1$, there are some trade-offs between K_f and n (Goren et al., 2014), which
 142 should not influence the main results of our modeling (Yuan et al., 2022).

143

144 **2.2 Two growth models for the Northeastern Tibetan Plateau**

145 We apply two double-stage growth models, including a two-block stage (block-block) growth
 146 model and a block-propagation growth model (Figure 3), to explore the ~20 Ma NETP growth
 147 history. The first model is consistent with the two-stage stepwise uplift in the NETP (Tapponnier
 148 et al., 2001). The latter model is inspired by various orogenic growth models, which suggest
 149 mountain belts growing to a certain height, and then expanding laterally in an outward growth

150 sequence characterized by a more successive marginal uplift (Jammes and Huismans, 2012; Wolf
 151 et al., 2022; Yuan et al., 2021), e.g., the outward growth of the Tibetan Plateau (Wang et al., 2014).
 152 The two growth models for the NETP with several free parameters simulate various uplift cases
 153 that predict different topographic evolutions (Figure 3). The two double-stage growth models for
 154 the NETP are likely the simplest plausible scenarios to produce our modeled results, without taking
 155 into account the complexities of the NETP, such as the influences of the strike-slip faults on the
 156 rock uplift (Tapponnier et al., 2001).

157 We use a logistic function of elevation (h_f) from the previous study (Yuan et al., 2021) to
 158 match the present-day maximum topography of the NETP as

$$159 \quad h_f(x, L) = \frac{h_0}{1+e^{[(x-L)/W]}}, \quad (2)$$

160 where h_0 is the present-day maximum elevation, W is the characteristic width of the plateau
 161 margin, L is the total length of the plateau, and x is the distance to the plateau margin.

162 For the first stage of block uplift (Figure 3a, b), the uplift rate is

$$163 \quad U_{1B} = (h_{1B}(x, L_{1B}) - h_i)/t_{1B}, \text{ with } h_{1B}(x, L_{1B}) = \frac{h_0}{1+e^{(x-L_{1B})/W}}, \quad (3)$$

164 where h_i is the initial elevation before the block uplift, L_{1B} and t_{1B} are the length and duration of
 165 the first block uplift stage, respectively. For the second stage of block uplift (Figure 3a), the uplift
 166 rate is

$$167 \quad U_{2B} = [h_f(x, L) - h_{1B}(x, L_{1B})]/t_{2B}, \quad (4)$$

168 where t_{2B} is the duration of the second block uplift stage. For the second stage of propagating
 169 uplift (Figure 3b), the uplift rate modified from Yuan et al. (2021) is

$$170 \quad U_{2P} = \frac{h_0 v_0 e^{(x-x_0)/W}}{W[1+e^{(x-x_0)/W}]^2}, \text{ with } x_0 = L_{1B} + v_0 t, \quad (5)$$

171 where x_0 and v_0 are the growth length and growth velocity ($v_0 = (L - L_{1B})/t_{2B}$), respectively.

172 The uplift rate U in equation (1) is replaced by U_{1B} , U_{2B} , and U_{2P} for the block growth and
 173 propagation growth model. According to the above equations, uplift rates (U_{1B} , U_{2B} , and U_{2P})
 174 depend much on the growth duration (t_{1B}) and distance (L_{1B}). Thus, there are only three free
 175 parameters (i.e., K_f , x_{1B} , and t_{1B}) for each growth model.

176

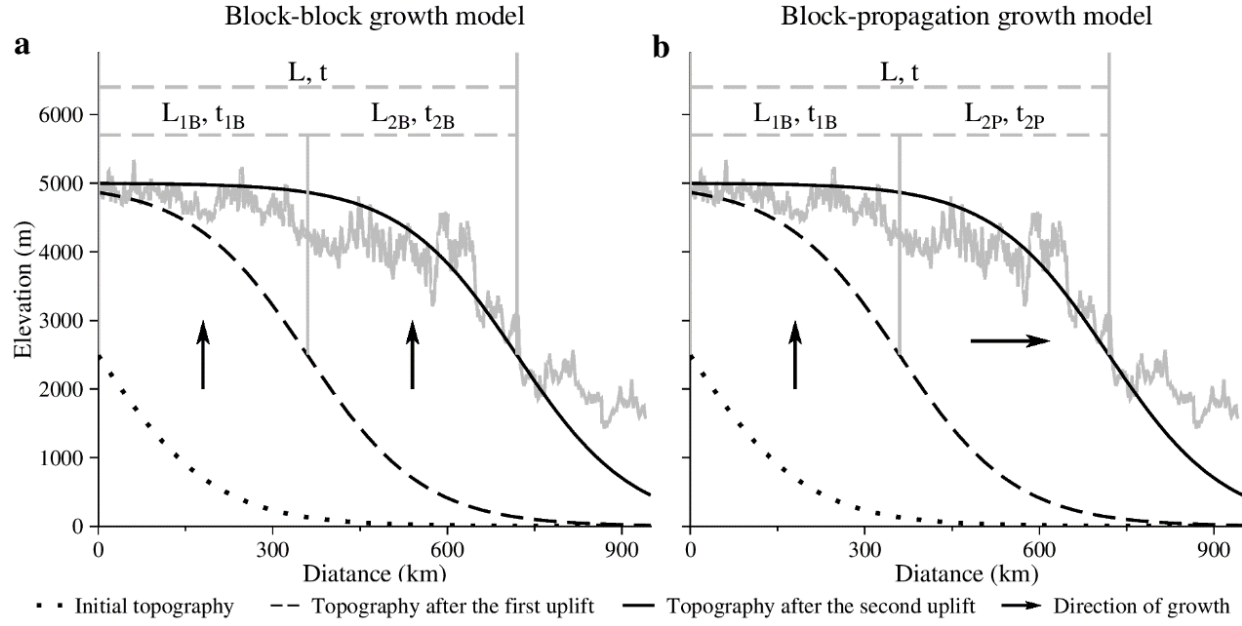


Figure 3. Diagrams for two growth models. (a) Block-block growth model. (b) Block-propagation growth model. Grey curves are the observed maximum topography within the blue shading area in Figure 1b. The present-day topography can be matched by a function in equation (2) (dark solid curve). L_{1B} and t_{1B} are the distance and duration of the first block growth, respectively. L_{2B} and t_{2B} are the distance and duration of the second block growth, respectively. L_{2P} and t_{2P} are the distance and duration of the second propagation growth, respectively. The block growth uplifts vertically, and the propagation model grows horizontally.

2.3 Model setup

In the NETP, the initially significant activity ages are younger than ~20 Ma (Figure 1b, c) (Duvall et al., 2013; Lease et al., 2011; Li et al., 2019, 2022; Yuan et al., 2011; Zhang et al., 1991; Zheng et al., 2006), and the modern high elevation was reached within ~23–11 Ma (Ding et al., 2022; Miao et al., 2022). Thus, we set the total growth duration of the two-stage uplift to 20 Myr ($t = t_1 + t_2 = 20$ Myr) cover the maximum growth age of the NETP. The total growth distance of the two-stage uplift is set to 720 km ($L = L_1 + L_2 = 720$ km) in our growth models, based on the present-day topography from the plateau interior to the plateau margin (near the Haiyuan Fault, Figure 1b, c).

To fit the present-day maximum topography of the NETP (equation 2), we set the maximum elevation to 5 km (i.e., $h_0 = 5$ km), and the characteristic width of propagation uplift to 100 km (i.e., $W = 100$ km). To model landscape evolution in the NETP, we define a rectangular domain

size of 950×600 km (Figure 1b) with each node size of 1×1 km, and run the model for 20 Myr. To increase modeling efficiency, we use a time step length of 100,000 years to find one of the best-fit models and a time step length of 10,000 years to extract information from the best-fit model. The modeled river profiles are similar by testing different time steps from 10,000 to 100,000 years (Figure S1). In the NETP, initial elevations (0-2500 m) with maximum elevations in the model south boundary (Figure 3) and random white noise (≤ 500 m) are assumed, based on the maximum elevations were $\sim 2500 \pm 500$ m at ~ 20 Ma near the south of the modeled area (Polissar et al., 2009; Sun et al., 2015).

206

207 2.4 Misfit function

The forward analyses of the landscape evolution model are used to explore the multidimensional space of free parameters (i.e., K_f , x_{1B} , and t_{1B}). Optimum values are found when the modeled river profile best matches the observed river profile of the UYR in the NETP. A parameter of χ was used to normalize the river profiles (Perron and Royden, 2013) at the point x :

$$213 \quad \chi(x) = \int_{x_b}^x \left(\frac{A_0}{A(x)} \right)^{m/n} dx, \quad (4)$$

where x_b is the base level (outlet: 750 km; Figure 1b), A_0 ($= 1$ m 2) is a reference drainage area, and $A(x)$ is the drainage area of the point x . We first calculate the observed χ_i^{obs} values of the UYR at each elevation bin h_i ($i = 1, 2, \dots, N$). Then, at the final step of the model, we obtain the modeled trunks (i.e., the longest channel of each modeled basin), and calculate the modeled χ_i^{mod} values at the corresponding elevation bin h_i .

219

220 **Table 1.** Free parameters range in the forward analysis.

Growth model	K_f ($\times 10^{-7}$ m $^{0.16}$ /yr)	L_{1B} (km)		t_{1B} (Myr)		
	Model range	Interval	Model range	Interval	Model range	Interval
Block-block growth model (Figure 3a)	15-41	2	0-700	100	0-20	1
Block-propagation growth model (Figure 3b)	15-41	2	0-700	100	0-20	1

221

222 An average misfit (μ) function compared the χ of modeled and observed river profiles:

223

$$\mu = \frac{1}{N_t} \sqrt{\frac{1}{N} \sum_{i=1}^N \frac{(\chi_i^{obs} - \chi_i^{mod})^2}{(\delta_x)^2}}, \quad (5)$$

224 where δ_x ($= 8$ m) is the uncertainty for the χ comparison set arbitrary, N_t is the total number of all
 225 modeled trunks in the final step. For each growth model, 2352 ($14 \times 8 \times 21$) forward process models
 226 are used to constrain the best-fit sets of three free parameters (Table 1).

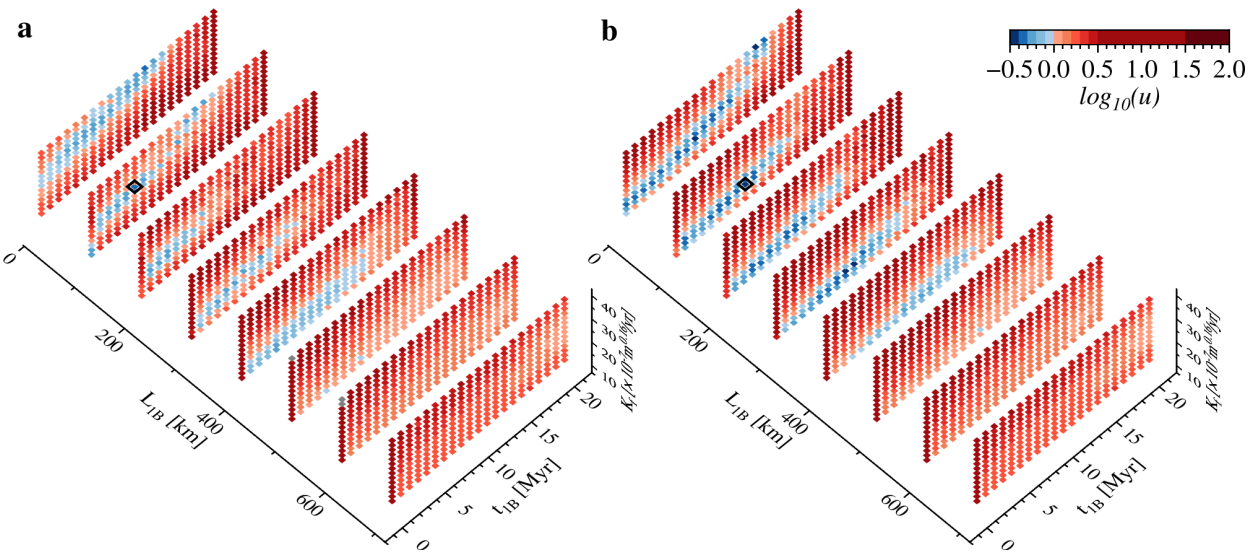
227

228 **3 Results**

229 We plot the misfit values μ ($\log_{10}(\mu) < 2.0$) of the two growth models for three free
 230 parameters (K_f , x_{1B} , and t_{1B}) with different colors (Figures 4 and S2). The best-fit value of the
 231 block-block growth model is higher than that of the block-propagation growth model. In the low
 232 $\log_{10}(\mu) < 0$ values (i.e., the best-fit models within uncertainty) of the block-block growth model,
 233 the distances (L_{1B}) and durations (t_{1B}) are less than 500 km and 15 Myr, respectively. The smallest
 234 $\log_{10}(\mu)$ value is -0.335 marked by the black box in Figure 4a ($K_f = 29 \times 10^{-7} \text{ m}^{0.16}/\text{yr}$, $L_{1B} =$
 235 100 km, and $t_{1B} = 5$ Myr). There is no modeled river profile (χ -elevation plots) matching well the
 236 observed river profile for the block-block growth model, even the best-fit modeled results (Figure
 237 5a). In the low $\log_{10}(\mu) < 0$ of the block-propagation growth model, the distances (L_{1B}) and the
 238 durations (t_{1B}) are less than 500 km and 17 Myr, respectively. The smallest $\log_{10}(\mu)$ value is
 239 -0.439 marked by the black box in Figure 4b ($K_f = 21 \times 10^{-7} \text{ m}^{0.16}/\text{yr}$, $L_{1B} = 100$ km, and $t_{1B} =$
 240 8 Myr). Several best-fit modeled river profiles matched the observed river profile well for the
 241 block-propagation growth model (Figure 5b).

242

Block-block growth model



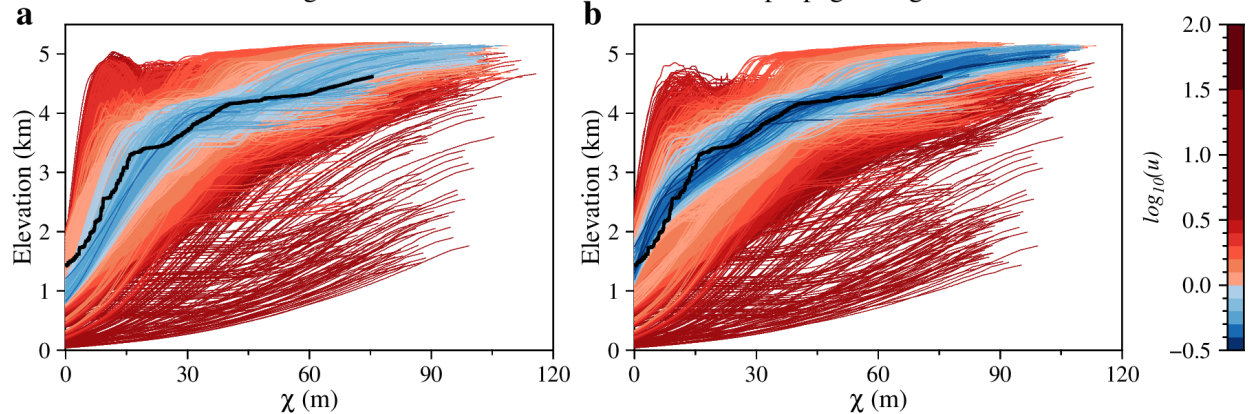
243

Figure 4. Modeled misfits of two growth models with each model 2352 forward analyses. (a) Block-block
244 growth model. A black box marks one of the best-fit parameter sets ($K_f = 29 \times 10^{-7} \text{ m}^{0.16}/\text{yr}$, $L_{1B} = 100$
245 km, and $t_{1B} = 5$ Myr), and the smallest $\log_{10}(\mu)$ value is -0.335 . (b) Block-propagation growth model. A
246 black box shows one of the best-fit parameter sets ($K_f = 21 \times 10^{-7} \text{ m}^{0.16}/\text{yr}$, $L_{1B} = 100$ km, and
247 $t_{1B} = 8$ Myr), and the smallest $\log_{10}(\mu)$ value is -0.439 .

248

249

Block-block growth model



250

Figure 5. Modeled (colored) and observed (black) river profiles are plotted by χ . (a) In the block-block
251 growth model, the modeled river profiles are less consistent with the observed river profile of the upstream
252 Yellow River. (b) In the block-propagation growth model, several modeled river profiles with dark blue
253 color matched well the observed river profile of the upstream Yellow River. The cooler the color, the lower
254 the misfit values, and the better the modeling results.

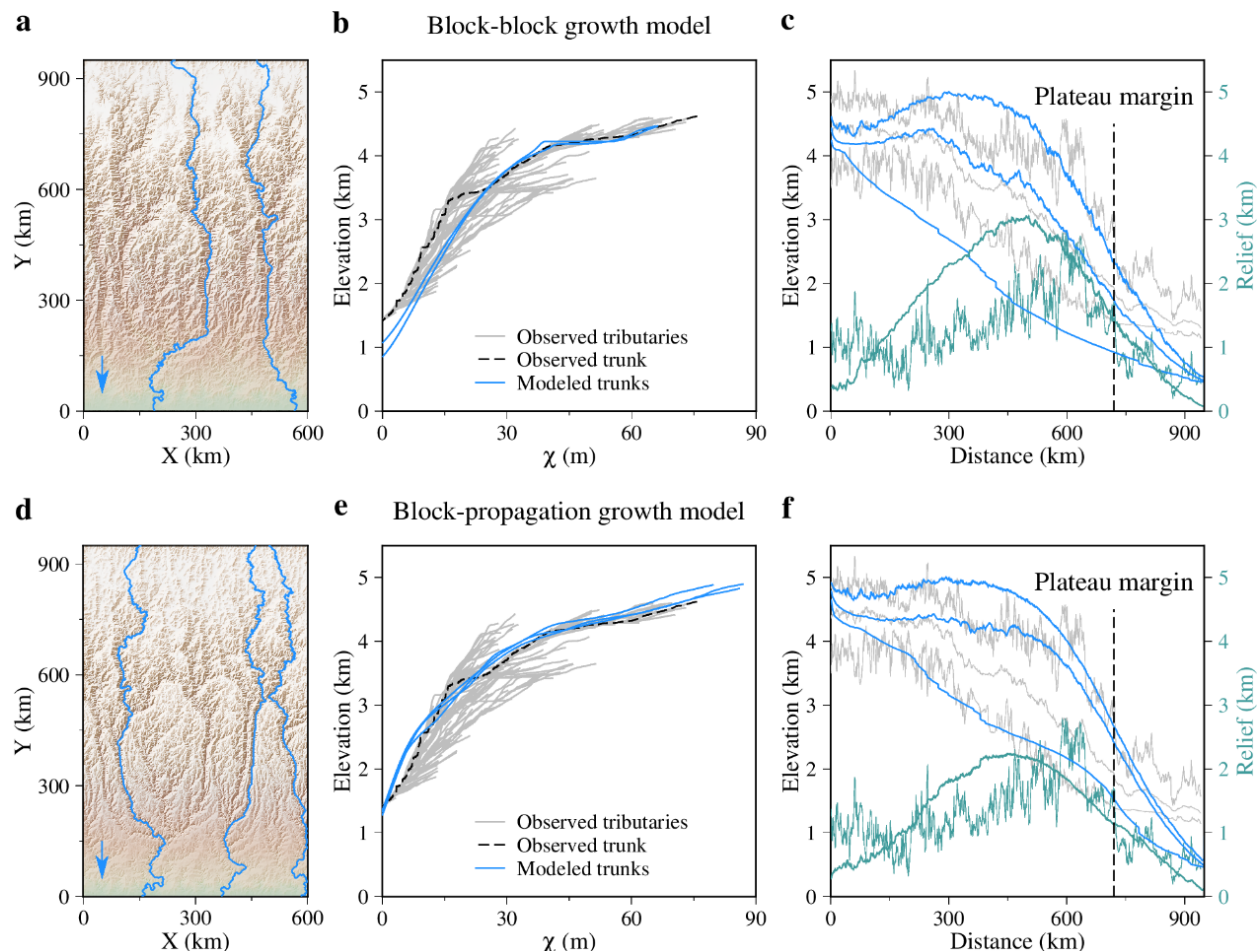
255

256

257 **4 Discussion**258 **4.1 The best-fit growth model of the Northeastern Tibetan Plateau**

259 This section compares one of the best-fit modeled results in each growth model to the
 260 observed results. χ -elevation plots are extracted from modeled trunks and the UYR. Although the
 261 modeled river profiles in each growth model are consistent with the upper reach of the observed
 262 river profile (with elevations >3500 m), only the modeled river profiles in the block-propagation
 263 growth model are consistent with the lower reach of the observed river profile (Figure 6b, e). In
 264 addition, the observed and modeled swath profiles of the block-propagation growth model are
 265 more consistent than that of the block-block growth model (Figure 6c, f).

266



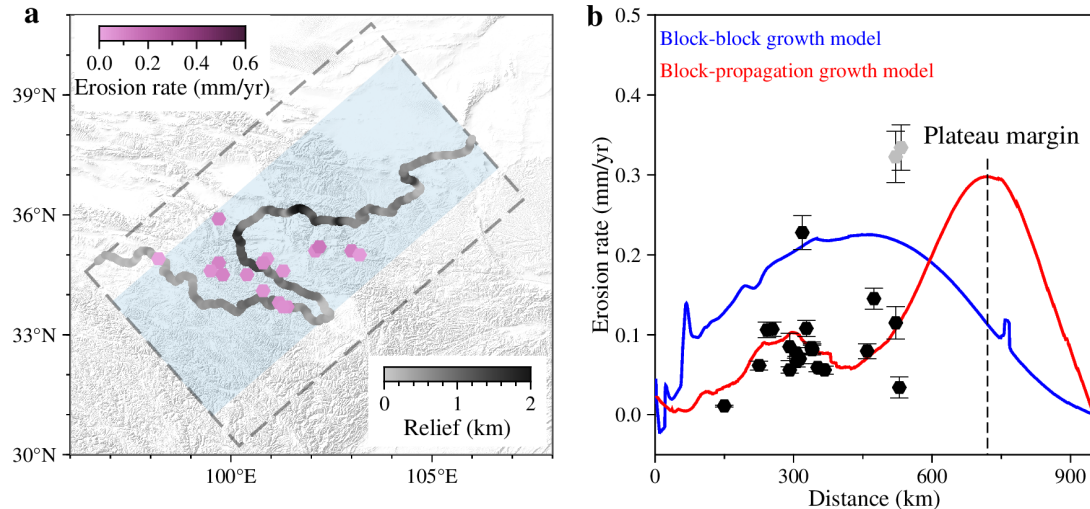
267

268 **Figure 6.** The comparison of geomorphic data between the best-fit model results of each growth model and
 269 the upstream Yellow River. (a, d) Modeled landscapes and trunks (blue lines). Blue arrows mark river
 270 directions. (b, e) χ -elevation plots. (c, f) Modeled and observed swaths and relief extracted from the whole

271 modeled domain and the blue shading area of the Northeastern Tibetan Plateau in Figure 1b, respectively.
272 The modeled trunks are the longest channels of each modeled basin. Grey and black lines are the observed
273 results, and blue lines are the modeled results in (b), (c), (e), and (f). In (c) and (f), green lines are the relief.
274

275 The modeled erosion rates and the trend of acceleration times of deformation are also
276 compared to the observed results. Modeled erosion rates from the block-propagation growth model
277 can better match most erosion rates from the plateau interior to the plateau margin (Figure 7b),
278 which is similar to the downstream increase of incision in the Daxia River ([Zhang et al., 2017a](#)), a
279 tributary of the UYR. Modeled age-elevation relationships show that only one synchronous
280 acceleration occurred in the block-block growth model (Figure 8b), which differs from the
281 observed various acceleration times of deformation (Figure 2). Examples include the East Kunlun
282 around 8-5 Ma ([Duvall et al., 2013](#)), the Dulan Chaka Highland around 17-12 Ma ([Duvall et al.,](#)
283 [2013](#)), the Laji Shan around 23-17 Ma ([Lease et al., 2011](#)), the Jishi Shan around 13-5 Ma ([Lease](#)
284 [et al., 2011](#)), the East Qilian Shan around 15-12 Ma ([Wang et al., 2020](#)), and the Liupan Shan
285 around 8-7 Ma ([Zheng et al., 2006](#)). In contrast, a northward progressive acceleration occurred in
286 the block-propagation growth model (Figure 8c), more consistent with the initially significant
287 activity ages which became younger to the northeast in the NETP (Figure 1c). Moreover, the
288 significant increasing uplift rate occurred after ~5 Ma near the plateau margin (~720 km) (Figure
289 8c), consistent with previous studies ([Zhang et al., 2023](#)). Thus, based on the comparisons of river
290 profiles, swath profiles, erosion rates, and the trend of significant acceleration times (e.g., initially
291 significant activity ages and thermochronometric age-elevation relationships), the block-
292 propagation growth model fits better with the NETP growth records.

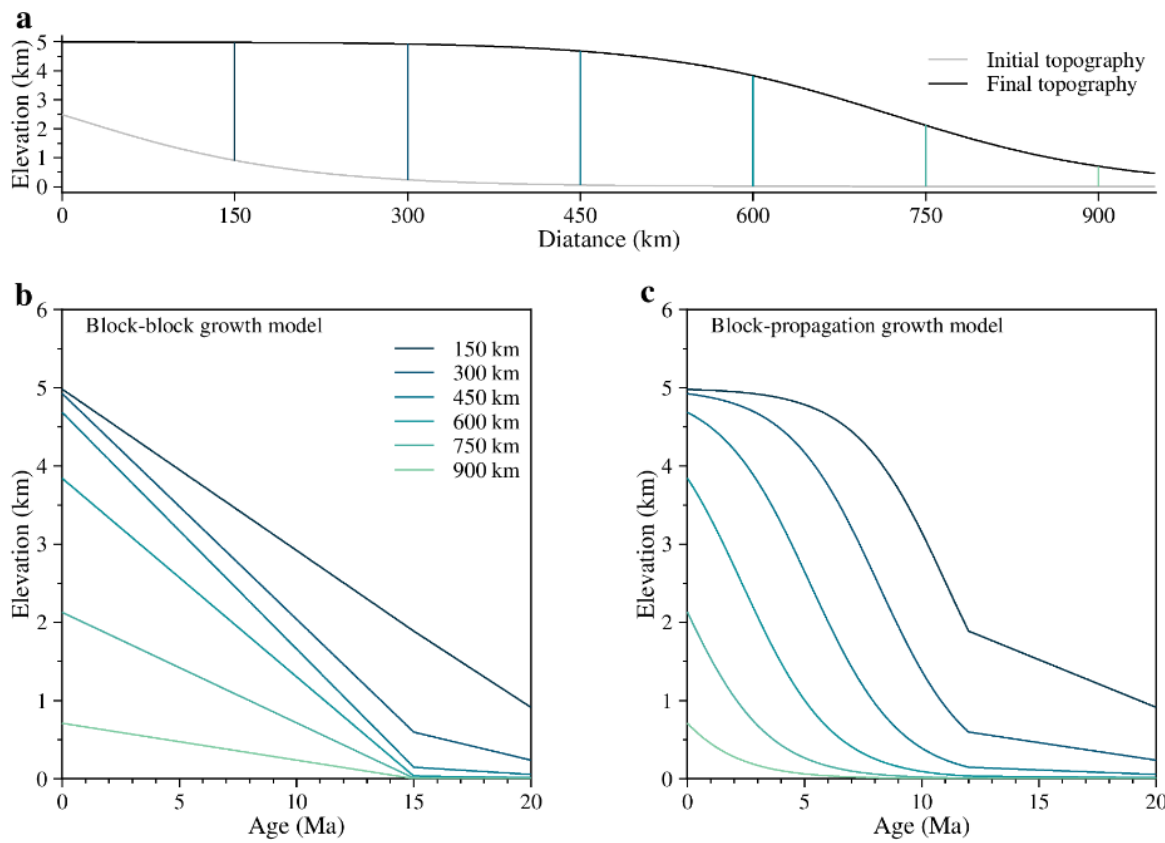
293



294

295 **Figure 7.** Comparison of the observed and modeled erosion rates. (a) Erosion rates distribution. (b)
 296 Comparisons of modeled erosion rates along the river profile. Erosion rates (Table S3) are from references
 297 (Harkins et al., 2007; Kirby and Harkins, 2013; Lal et al., 2004; Li et al., 2014b; Zhang et al., 2017a). Grey
 298 dots are influenced by transient sediments (Zhang et al., 2017a).

299



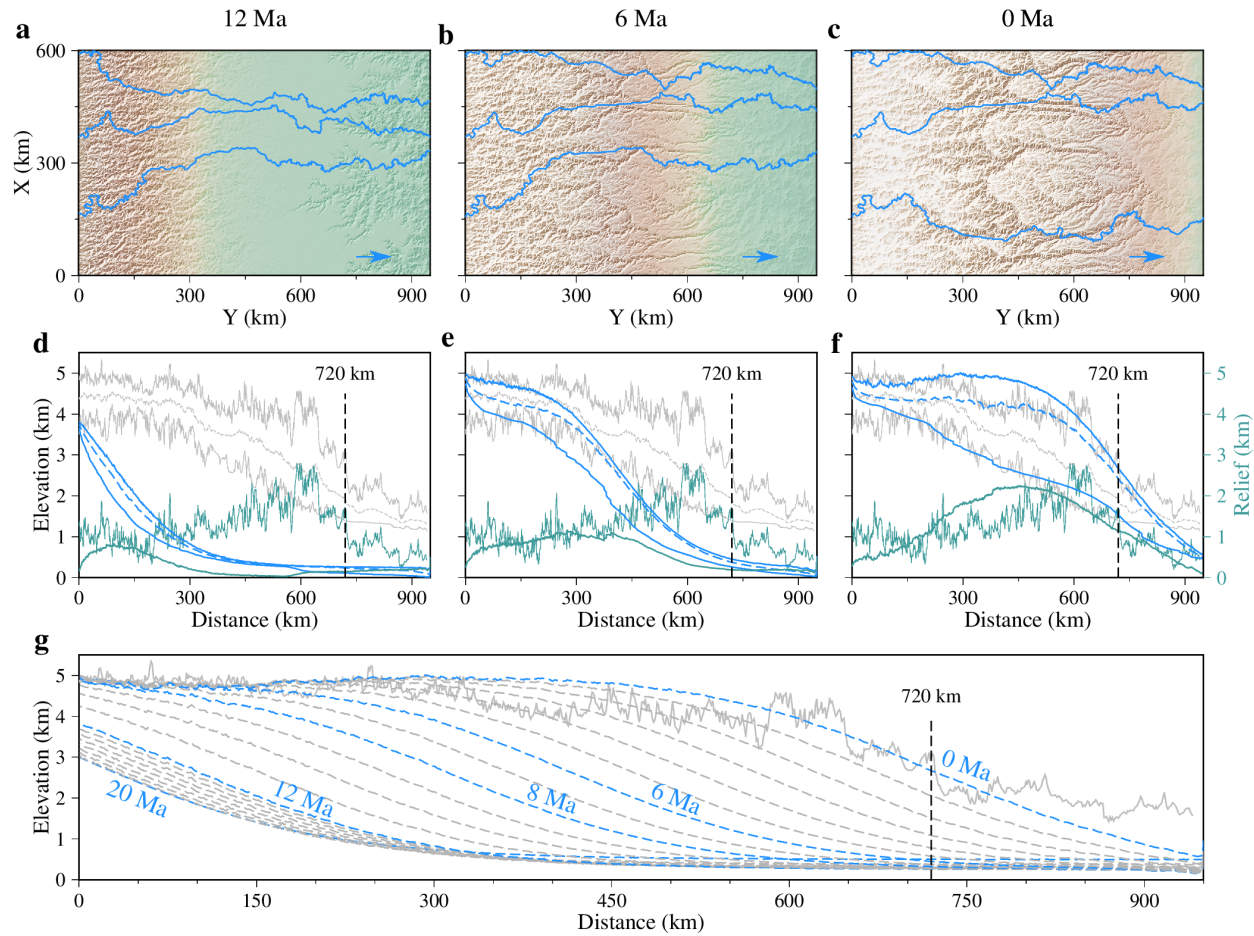
300

301 **Figure 8.** Modeled age-elevation relationships of two growth models. (a) Location of different distances.
 302 (b) Block-block growth model. (c) Block-propagation growth model.

303 **4.2 Growth history of the Northeastern Tibetan Plateau**

304 Based on our forward analyses, the block-propagation growth model matches better the NETP
 305 growth records. The major range of block uplift only occurred in the south of the modeled area
 306 before \sim 12 Ma (middle Miocene), with broad low elevations in most of the modeled area (Figure
 307 9). Then, a broad propagation uplift occurred in the modeled area from \sim 12 Ma to the present,
 308 forming the modern plateau margin (Figure 9). High elevations (\sim 5 km) expand northward during
 309 the plateau growth (Figure 9g).

310

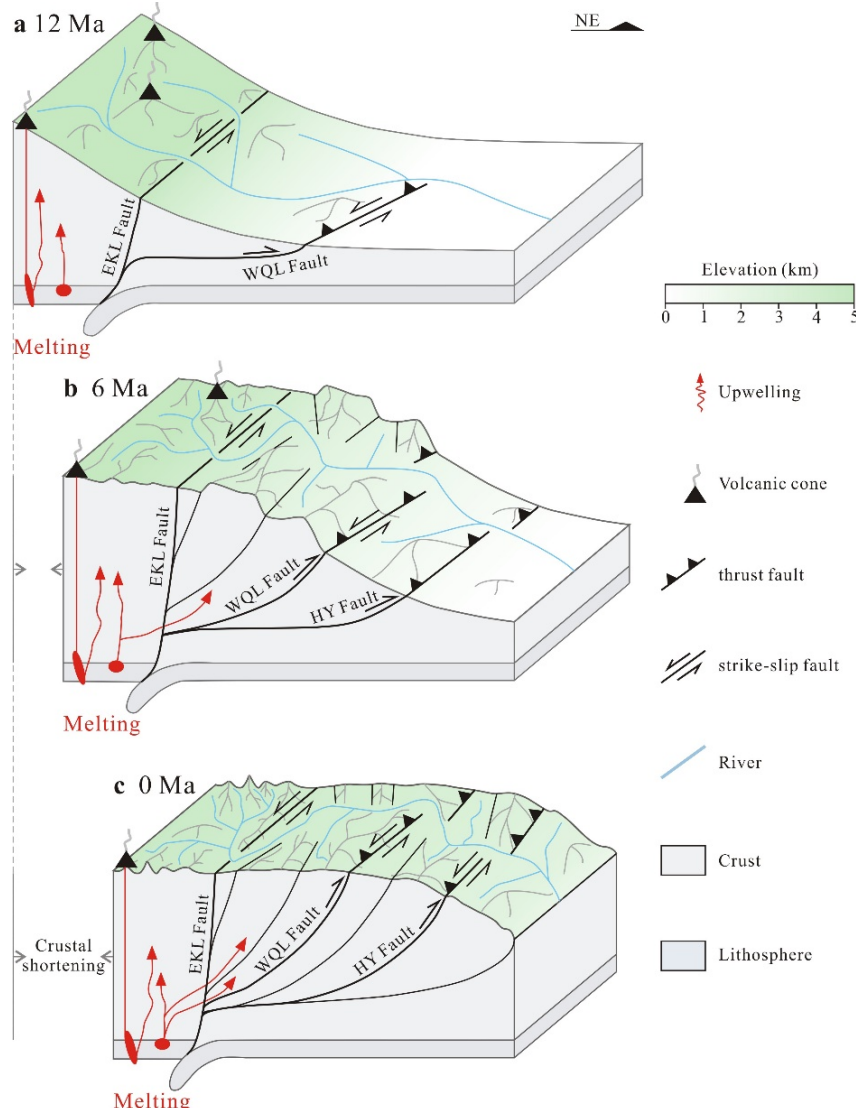


311

312 **Figure 9.** Typical modeled scenarios of the block-propagation growth model. Top panels are modeled
 313 landscapes and trunks (blue) at (a) 12 Ma, (b) 6 Ma, and (c) 0 Ma. Blue arrows mark river directions. Middle
 314 panels are observed (grey) and modeled (blue) swath profiles and relief (green) at (d) 12 Ma, (e) 6 Ma, and
 315 (f) 0 Ma. (g) The bottom panel shows the maximum elevations along modeled trunks during uplifting.
 316 Dashed lines are modeled maximum elevations from 20 Ma to 0 Ma. A grey continuous line is the observed
 317 maximum elevation at 0 Ma. The black dashed line at 720 km in (d), (e), (f), and (g) indicates the plateau
 318 margin.

Our modeled data are consistent with various observed data, including crustal deformations (Fan et al., 2019; Royden et al., 2008; Yan et al., 2006; Yu et al., 2023) and sedimentary records (Chang et al., 2015; Li et al., 2011). For example, most initial faulting ages in the NETP were after ~20 Ma, with a northward younging trend (Figure 1b, c). The initial propagation uplift time (~12 Ma) is consistent with the widespread middle-Miocene crustal deformation in the NETP (Yu et al., 2023), the formation time (Miocene) of basin-bounding faults in the NETP and the eastern segment of the NETP (Fan et al., 2019). The propagation uplift time of ~12 Ma is also consistent with most of the shortening after ~15 to 20 Ma in the NETP (Royden et al., 2008), and a clockwise rotation during 11-17 Ma in the Guide Basin (Figure 1b) (Yan et al., 2006) based on the magnetostratigraphy. The initial propagation uplift time is also close to the accumulation rate abruptly increased near ~15 Ma in the Qaidam Basin (Figure 1b) based on a stratigraphic study (Chang et al., 2015), and the progressive surface uplift since 15 Ma in the NETP based on the Nd isotopic ratio of Asian dust (Li et al., 2011).

We show the major block uplift and higher elevations occurring in the south of the NETP before ~12 Ma, with broad low elevations to the north, consistent with the observed higher elevations in the south (Polissar et al., 2009; Sun et al., 2015) and low elevations in the north of the East Kunlun fault (Hui et al., 2018). The Hoh-Xil Basin (upper part of the UYR, Figure 1b) reached 1395-2931 m before 17 Ma based on the leaf fossils from an early Miocene barberry (*Berberis*) (Sun et al., 2015), or had uplifted at least 1700-2600 m before the middle Miocene based on δD ratio of surface waters from freshwater limestones (Polissar et al., 2009). In contrast, the Zeku Basin (lower part of the UYR, Figure 1b) had 1200-1400 m elevations during the early to middle Miocene based on palynological data (Hui et al., 2018). Our results are also consistent with the observations of the south of the East Kunlun Fault (Hoh Xil Basin) reached 2-3 km before the Miocene and the modern high elevation of ~4.6 km after ~17 Ma (Staisch et al., 2016). The Hoh Xil Basin had probably reached its current elevation of ~4.6 km by ~12 Ma, considering possible uncertainties (Li and Garzione, 2023). The north of the East Kunlun Fault reached the modern high elevations after ~11 Ma (Miao et al., 2022), based on the pollen records of montane conifers. The surface uplift is not synchronous but is progressive to the north, consistent with our modeling (Figure 9g).



348

349 **Figure 10.** Schematic models illustrate different growth mechanisms on both sides of the East Kunlun
 350 Fault. (a) The scenario occurred after block growth (12 Ma) with higher elevations in the south of the East
 351 Kunlun Fault than in the north. (b) Propagation growth at 6 Ma. (c) Schematic present-day topography (0
 352 Ma). The hypothetical elevations in the diagrams are based on the uplift process in Figure 9g. Initial
 353 significant activity ages are based on the data in Figure 1b. EKL Fault: East Kunlun Fault; WQL Fault:
 354 West Qinling Fault; HY Fault: Haiyuan Fault. Deep structures are modified from [Tapponnier et al. \(2001\)](#).
 355 Primary faults in the NETP are modified from references ([Tapponnier et al., 2001](#); [Yuan et al., 2013](#)).
 356

357 Different uplift processes in the south and north of the East Kunlun Fault may be related to
 358 different uplift mechanisms ([Chen et al., 2017](#); [Lease et al., 2012](#); [Staisch et al., 2016](#); [Tapponnier et al., 1990](#)) (Figure 10). The East Kunlun Fault is an important rheological boundary ([Karplus et](#)

360 al., 2011; Le Pape et al., 2012), based on a magnetotelluric profile crossing the Northern Tibetan
361 Plateau (Unsworth et al., 2004). Because of different growth processes in the south and north of
362 the East Kunlun fault, a Paleogene basin was partitioned into the Hoh Xil and Qaidam subbasins
363 by the East Kunlun fault before the middle Miocene (Chen et al., 2017; Yin et al., 2008). In the
364 south of the East Kunlun Fault, the upper crustal shortening within the Hoh Xil Basin ceased
365 between 33.5 and 27.3 Ma (Staisch et al., 2016), and the crust thickening driven by mantle removal
366 related to partial melting or mantle melting (Chen et al., 2017; Staisch et al., 2016) played an
367 important role in the plateau growth since the Miocene (Figure 10a). The surface has been raised
368 ~2 km by mantle melting since the early Miocene (25-20 Ma) (Chen et al., 2017). The magmatic
369 activities widely occurred in the south of the East Kunlun Fault, related to opposing north-directed
370 and south-directed continental subduction after 25 Ma (Guo and Wilson, 2019). In contrast,
371 magmatic activities were rare in the north of the East Kunlun Fault (Yin and Harrison, 2000).

372 In the north of the East Kunlun Fault, some researchers suggest that the partial melt
373 penetration probably characterizes the plateau growth (Karplus et al., 2011; Medvedev et al.,
374 2006), but crust thickening driven by shortening played a critical role in forming the NETP through
375 fault thrusting and folding (Hu et al., 2015; Lease et al., 2012; Tapponnier et al., 1990) (Figure
376 10b, c). A transition of the tectonic regime, from extrusion to the distributed shortening in the
377 Northern Tibetan Plateau, was initiated at ~15 Ma (Lu et al., 2016). The distributed crustal
378 shortening was one of the dominant processes in the Northern Tibetan Plateau construction (Zuza
379 et al., 2016). For example, the Jishi Shan, between the Kunlun and Haiyuan left-lateral faults,
380 experienced accelerated exhumation due to thrust-induced rock uplift and erosion at ~13 Ma based
381 on thermochronological data (Lease et al., 2011). More than half of net Cenozoic crustal shortening
382 and thickening in this area has occurred since ~13 Ma, based on cross-section reconstructions
383 (Lease et al., 2012). A reconstruction of crustal thickness around the Jishi Shan shows the crust
384 thickening from the middle Miocene thickness of 50 ± 4 km to the modern thickness of 56 ± 4 km
385 (Lease et al., 2012). In addition, most of the present elevations were reached since the middle
386 Miocene in the NETP (Hui et al., 2018; Zhuang et al., 2014). In the Zeku basin (Figure 1b), the
387 present 60-70% elevations were mainly uplifted since the early-middle Miocene, based on
388 palynological data in the Caergen section (Hui et al., 2018). The Qaidam Basin, near the UYR,
389 whose present elevations of 70% were uplifted during 15-10.4 Ma, based on Leaf wax stable
390 isotopes in the Huaitoutala section (Zhuang et al., 2014).

391 In summary, consistent with the above studies, our modeled results suggest that most present-
392 day high elevations (~5 km) have been reached since the middle Miocene in the north of the East
393 Kunlun Fault, and then the high elevations expanded northward. The plateau uplift is mostly
394 attributed to the crustal thickening, and the gradual propagation was related to the crustal
395 shortening through fault thrusting and folding.

396

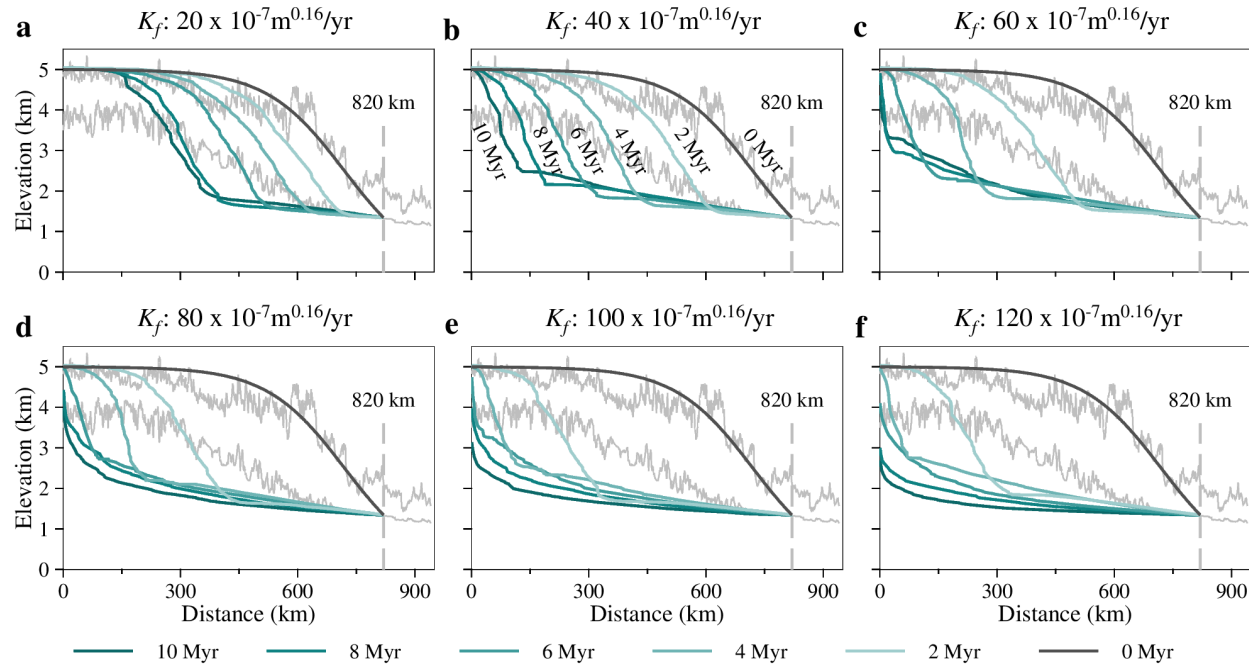
397 **4.3 Headward erosion cannot form the observed upstream Yellow River profile**

398 The NETP growth primarily controls the UYR formation. However, the UYR formation time
399 is debated, varying from >11.63 Ma to >0.03 Ma based on the initial incision timing (~1.8-0.03
400 Ma) of the upmost terraces (Craddock et al., 2010), the dating of basin sediments (~1.7 Ma) (Li et
401 al., 2014a), the similar provenance signals in the Linxia and Lanzhou Basins (Figure 1b) (~3.6
402 Ma) (Nie et al., 2015), the isolation time (1.2-0.5 Ma) of the Qinghai Lake (Figure 1b) (Zhang et
403 al., 2014), the divergence time (~0.19 Ma) of two species (Liang et al., 2018), the sediment in the
404 Hetao Basin (Figure 1b) (~1.68 Ma) (Li et al., 2023), the termination time (~4.8 Ma) of
405 fluviolacustrine-dominated red beds in the Xining Basin (Figure 1b) (Zhang et al., 2017b), and the
406 initial sedimentation (>11.63 Ma) of Eocene-Miocene red bed in the Lanzhou zone (Lin et al.,
407 2001). Among these formation timings, some studies suggest that the UYR formed over the last
408 few million years (~2.58-0.03 Ma) since the UYR excavated basin sediments systematically
409 upstream through headward erosion (Craddock et al., 2010; Jia et al., 2017; Su et al., 2023), with
410 a rate of ~350 km Myr⁻¹ (Craddock et al., 2010). The block-block growth model experiences
411 headward erosion in our study because the modeled area only grows upward without horizontal
412 motion. χ -elevation plots from all block-block growth models, compared to the UYR river profile,
413 show that no appropriate modeled results can match the observed UYR river profile (Figure 5a).
414 In contrast, a few block-propagation growth model results match the observed UYR river profile
415 (Figure 5b). The high erosion rates mainly propagated downstream during the outward propagation
416 of the NETP growth, similar to the erosion pattern that occurred in the eastern Tibetan Plateau
417 (Yuan et al., 2023).

418 Next, we test whether the pure headward erosion (and retreat process) can form the UYR
419 river profile using the landscape evolution model with various erodibilities and model run
420 durations. To match the elevation of the observed base level of the NETP margin, we set the
421 modeled boundary at 820 km (Figure 11). The initial topography is set to the maximum topography

(Figure 3) based on equation 2, with the amplitude white noise (<100 m). The fluvial erodibilities are set to $(2, 4, 6, 8, 10, \text{ and } 12) \times 10^{-6} \text{ m}^{0.16}/\text{yr}$, and the model run durations are set to (2, 4, 6, 8, and 10) Myr for modeling the retreat process (Figure 11). Modeled river profiles (Figure 5a, 11) indicate that the pure headward erosion suggested by previous studies (Craddock et al., 2010; Harkins et al., 2007; Jia et al., 2017; Su et al., 2023) hardly formed the UYR river profile over a few million years.

428



429

Figure 11. The observed maximum and minimum elevations (grey) and modeled (thick line) river profiles from different sets of erodibilities and model durations in each headward erosion and retreat process. We set the modeled boundary at 820 km to match the elevation of the observed and modeled base levels.

433

Most young formation times of the UYR are suggested based on the abandonment time (i.e., initial incision time) of the upmost terraces (Craddock et al., 2010; Jia et al., 2017; Su et al., 2023; Zhang et al., 2014). However, the divergent young ages for the inception of the Yellow River can be related to periodic climate fluctuations, and may correspond only to different re-integration events due to deglaciation or desiccation (Zhao et al., 2023). The re-integration events due to desiccation have been reported in the Yellow River middle reach (Zhao et al., 2023). In addition, the formation, abandonment, and preservation of fluvial terraces are often related to changes in tectonics and/or climate (Reusser et al., 2004; Wang et al., 2015). Modifying any external factors

442 can rework the previously formed fluvial terraces and erase the previous geomorphic and
443 stratigraphic records (Pan et al., 2009), and the hoarier records of fluvial terraces may be modified
444 more easily.

445 On the other hand, the thermochronometric age-elevation relationships (Figure 2), responding
446 to a long-term history of exhumation, suggest that the NETP experienced a long-term exhumation
447 history, rather than a short-term erosion history over a few million years. Moreover, there were
448 connections between the upstream mountain and the downstream basin before 20 Ma in the NETP
449 (Liu, 2015). Sediments from the Anyemaqen Shan (Figure 1b) were deposited in the Guide Basin
450 during 53-33 Ma and in the Lanzhou Basin around 43 Ma (Liu, 2015). In summary, we suggest
451 that the UYR may have existed long accompanying the long-term NETP growth, based on our
452 modeled results, previous studies, and thermochronometric data.

453

454 **5 Conclusions**

455 Using a numerical landscape evolution model, we quantitatively study the ~20 Ma growth
456 history of the NETP correlated with the formation of the UYR. The block-propagation growth
457 model, comprised of an early block uplift (~20-12 Ma) and a late propagation uplift (~12-0 Ma),
458 is consistent with the records of the NETP based on the comparisons of the observed and modeled
459 river profiles, swath profiles, erosion rates, the trend of acceleration times of deformation (e.g.,
460 initially significant activity ages and thermochronometric age-elevation relationships), and paleo-
461 elevation datasets. We show that a block growth primarily occurred in the south of the NETP
462 before ~12 Ma (middle Miocene), and a propagation growth broadly occurred in the NETP after
463 ~12 Ma with high elevations (~5 km) expanding northward. We further suggest that pure headward
464 erosion unlikely formed the river profile of the UYR over a few million years. Our results show
465 that the long-term fluvial erosion in the NETP features mainly a downstream migration of high
466 erosion rates, which is significantly different from the headward erosion of small mountain rivers.
467 This erosion pattern in the NETP, similar to that occurred in the Eastern Tibetan Plateau (Yuan et
468 al., 2023), may represent a common erosion pattern of outward-growing plateaus in tectonically
469 active regions on Earth.

470

471 **Acknowledgments**

472 We thank XXX for reviewing. X.P.Y. acknowledges funding from NSFC (Grant 42272261).

473 **Data Availability Statement**

474 The codes used for the simulations are available in [Yuan et al. \(2019\)](#) and
475 <https://doi.org/10.5281/zenodo.3833983> website ([Bovy & Braun, 2020](#)). Figures were made using
476 ParaView, CorelDRAW, and Generic Mapping Tools.

477

478 **References**

- 479 Allen, P. A. (2008), From landscapes into geological history: *Nature*, 451 (7176), 274-276. Doi: 10.1038/nature06586.
480 An, Z., Kutzbach, J. E., Prell, W. L., & Porter, S. C. (2001), Evolution of Asian monsoons and phased uplift of the
481 Himalaya–Tibetan plateau since Late Miocene times: *Nature*, 411 (6833), 62-66. Doi: 10.1038/35075035.
482 Bovy, B., & Braun, J. (2020). Fastscape-lem/fastscapelib-fortran. Zenodo. Doi: 10.5281/zenodo.3833983.
483 Braun, J., & Willett, S. D. (2013), A very efficient O(n), implicit and parallel method to solve the stream power
484 equation governing fluvial incision and landscape evolution: *Geomorphology*, 180-181 (170-179). Doi:
485 10.1016/j.geomorph.2012.10.008.
486 Chang, H., Li, L., Qiang, X., Garzione, C. N., Pullen, A., & An, Z. (2015), Magnetostratigraphy of Cenozoic deposits
487 in the western Qaidam Basin and its implication for the surface uplift of the northeastern margin of the Tibetan
488 Plateau: *Earth and Planetary Science Letters*, 430 (271-283. Doi: 10.1016/j.epsl.2015.08.029.
489 Chen, J.-L., Yin, A., Xu, J.-F., Dong, Y.-H., & Kang, Z.-Q. (2017), Late Cenozoic magmatic inflation, crustal
490 thickening, and >2 km of surface uplift in central Tibet: *Geology*, 46 (1), 19-22. Doi: 10.1130/g39699.1.
491 Clark, M. K., Farley, K. A., Zheng, D., Wang, Z., & Duvall, A. R. (2010), Early Cenozoic faulting of the northern
492 Tibetan Plateau margin from apatite (U–Th)/He ages: *Earth and Planetary Science Letters*, 296 (1-2), 78-88. Doi:
493 10.1016/j.epsl.2010.04.051.
494 Clark, M. K., & Royden, L. H. (2000), Topographic ooze: Building the eastern margin of Tibet by lower crustal flow:
495 *Geology*, 28 (8), 703-706. Doi: 10.1130/0091-7613(2000)28<703:Tobtem>2.0.Co;2.
496 Craddock, W. H., Kirby, E., Harkins, N. W., Zhang, H., Shi, X., & Liu, J. (2010), Rapid fluvial incision along the
497 Yellow River during headward basin integration: *Nature Geoscience*, 3 (3), 209-213. Doi: 10.1038/ngeo777.
498 Dai, S., Fang, X., Dupont-Nivet, G., Song, C., Gao, J., Krijgsman, W., Langereis, C., & Zhang, W. (2006),
499 Magnetostratigraphy of Cenozoic sediments from the Xining Basin: Tectonic implications for the northeastern
500 Tibetan Plateau: *Journal of Geophysical Research: Solid Earth*, 111 (B11). Doi: 10.1029/2005JB004187.
501 Dayem, K. E., Molnar, P., Clark, M. K., & Houseman, G. A. (2009), Far-field lithospheric deformation in Tibet during
502 continental collision: *Tectonics*, 28 (6). Doi: 10.1029/2008TC002344.
503 Ding, L., Kapp, P., Cai, F., Garzione, C. N., Xiong, Z., Wang, H., & Wang, C. (2022), Timing and mechanisms of
504 Tibetan Plateau uplift: *Nature Reviews Earth & Environment*, 3 (10), 652-667. Doi: 10.1038/s43017-022-00318-
505 4.
506 Dupont-Nivet, G., Horton, B. K., Butler, R. F., Wang, J., Zhou, J., & Waanders, G. L. (2004), Paleogene clockwise
507 tectonic rotation of the Xining-Lanzhou region, northeastern Tibetan Plateau: *Journal of Geophysical Research:*
508 *Solid Earth*, 109 (B4). Doi: 10.1029/2003JB002620.

- 509 Duvall, A. R., Clark, M. K., Kirby, E., Farley, K. A., Craddock, W. H., Li, C., & Yuan, D.-Y. (2013), Low-temperature
510 thermochronometry along the Kunlun and Haiyuan Faults, NE Tibetan Plateau: Evidence for kinematic change
511 during late-stage orogenesis: *Tectonics*, 32 (5), 1190-1211. Doi: 10.1002/tect.20072.
- 512 England, P., & Houseman, G. (1989), Extension during continental convergence, with application to the Tibetan
513 Plateau: *Journal of Geophysical Research*, 94 (B12). Doi: 10.1029/JB094iB12p17561.
- 514 Fan, L.-G., Meng, Q.-R., Wu, G.-L., Wei, H.-H., Du, Z.-M., & Wang, E. (2019), Paleogene crustal extension in the
515 eastern segment of the NE Tibetan plateau: *Earth and Planetary Science Letters*, 514 (62-74. Doi:
516 10.1016/j.epsl.2019.02.036.
- 517 Fang, X., Dupont-Nivet, G., Wang, C., Song, C., Meng, Q., Zhang, W., Nie, J., Zhang, T., Mao, Z., & Chen, Y. (2020),
518 Revised chronology of central Tibet uplift (Lunpola Basin): *Science Advances*, 6 (50), eaba7298. Doi:
519 10.1126/sciadv.aba7298.
- 520 Fox, M., Bodin, T., & Shuster, D. L. (2015), Abrupt changes in the rate of Andean Plateau uplift from reversible jump
521 Markov Chain Monte Carlo inversion of river profiles: *Geomorphology*, 238 (1-14. Doi:
522 10.1016/j.geomorph.2015.02.022.
- 523 Goren, L., Fox, M., & Willett, S. D. (2014), Tectonics from fluvial topography using formal linear inversion: Theory
524 and applications to the Inyo Mountains, California: *Journal of Geophysical Research: Earth Surface*, 119 (8),
525 1651-1681. Doi: 10.1002/2014jf003079.
- 526 Guerit, L., Yuan, X.-P., Carretier, S., Bonnet, S., Rohais, S., Braun, J., & Rouby, D. (2019), Fluvial landscape evolution
527 controlled by the sediment deposition coefficient: Estimation from experimental and natural landscapes: *Geology*,
528 47 (9), 853-856. Doi: 10.1130/g46356.1.
- 529 Guo, Z., & Wilson, M. (2019), Late Oligocene–early Miocene transformation of postcollisional magmatism in Tibet:
530 *Geology*, 47 (8), 776-780. Doi: 10.1130/g46147.1.
- 531 Guo, Z., Wilson, M., Dingwell, D. B., & Liu, J. (2021), India-Asia collision as a driver of atmospheric CO₂ in the
532 Cenozoic: *Nature Communications*, 12 (1), 3891. Doi: 10.1038/s41467-021-23772-y.
- 533 Harkins, N., Kirby, E., Heimsath, A., Robinson, R., & Reiser, U. (2007), Transient fluvial incision in the headwaters
534 of the Yellow River, northeastern Tibet, China: *Journal of Geophysical Research: Earth Surface*, 112 (F3). Doi:
535 10.1029/2006JF000570.
- 536 Hu, X., Pan, B., Kirby, E., Gao, H., Hu, Z., Cao, B., Geng, H., Li, Q., & Zhang, G. (2015), Rates and kinematics of
537 active shortening along the eastern Qilian Shan, China, inferred from deformed fluvial terraces: *Tectonics*, 34
538 (12), 2478-2493. Doi: 10.1002/2015tc003978.
- 539 Hui, Z., Li, X., Ma, Z., Xiao, L., Zhang, J., & Chang, J. (2018), Miocene pollen assemblages from the Zeku Basin,
540 northeastern Tibetan Plateau, and their palaeoecological and palaeoaltimetric implications: *Palaeogeography,*
541 *Palaeoclimatology, Palaeoecology*, 511 (419-432. Doi: 10.1016/j.palaeo.2018.09.009.
- 542 Jammes, S., & Huismans, R. S. (2012), Structural styles of mountain building: Controls of lithospheric rheologic
543 stratification and extensional inheritance: *Journal of Geophysical Research: Solid Earth*, 117 (B10). Doi:
544 10.1029/2012JB009376.
- 545 Jia, L., Hu, D., Wu, H., Zhao, X., Chang, P., You, B., Zhang, M., Wang, C., Ye, M., Wu, Z., & Liang, X. (2017), Yellow

- 546 River terrace sequences of the Gonghe–Guide section in the northeastern Qinghai–Tibet: Implications for plateau
547 uplift: *Geomorphology*, 295 (323-336. Doi: 10.1016/j.geomorph.2017.06.007.
- 548 Karplus, M. S., Zhao, W., Klemperer, S. L., Wu, Z., Mechie, J., Shi, D., Brown, L. D., & Chen, C. (2011), Injection
549 of Tibetan crust beneath the south Qaidam Basin: Evidence from INDEPTH IV wide-angle seismic data: *Journal*
550 *of Geophysical Research*, 116 (B7). Doi: 10.1029/2010jb007911.
- 551 Kirby, E., & Harkins, N. (2013), Distributed deformation around the eastern tip of the Kunlun fault: *International*
552 *Journal of Earth Sciences*, 102 (7), 1759-1772. Doi: 10.1007/s00531-013-0872-x.
- 553 Kirby, E., Whipple, K. X., Tang, W., & Chen, Z. (2003), Distribution of active rock uplift along the eastern margin of
554 the Tibetan Plateau: Inferences from bedrock channel longitudinal profiles: *Journal of Geophysical Research:*
555 *Solid Earth*, 108 (B4). Doi: 10.1029/2001jb000861.
- 556 Klaus, S., Morley, R. J., Plath, M., Zhang, Y.-P., & Li, J.-T. (2016), Biotic interchange between the Indian subcontinent
557 and mainland Asia through time: *Nature Communications*, 7 (1), 12132. Doi: 10.1038/ncomms12132.
- 558 Kutzbach, J. E., Prell, W. L., & Ruddiman, W. F. (1993), Sensitivity of Eurasian Climate to Surface Uplift of the
559 Tibetan Plateau: *The Journal of Geology*, 101 (2), 177-190. Doi: [10.1086/648215](https://doi.org/10.1086/648215).
- 560 Lal, D., Harris, N. B. W., Sharma, K. K., Gu, Z., Ding, L., Liu, T., Dong, W., Caffee, M. W., & Jull, A. J. T. (2004),
561 Erosion history of the Tibetan Plateau since the last interglacial: constraints from the first studies of cosmogenic
562 ¹⁰Be from Tibetan bedrock: *Earth and Planetary Science Letters*, 217 (1), 33-42. Doi: 10.1016/S0012-
563 821X(03)00600-9.
- 564 Law, R., & Allen, M. B. (2020), Diachronous Tibetan Plateau landscape evolution derived from lava field
565 geomorphology: *Geology*, 48 (3), 263-267. Doi: 10.1130/g47196.1.
- 566 Le Pape, F., Jones, A. G., Vozar, J., & Wenbo, W. (2012), Penetration of crustal melt beyond the Kunlun Fault into
567 northern Tibet: *Nature Geoscience*, 5 (5), 330-335. Doi: 10.1038/ngeo1449.
- 568 Lease, R. O., Burbank, D. W., Clark, M. K., Farley, K. A., Zheng, D., & Zhang, H. (2011), Middle Miocene
569 reorganization of deformation along the northeastern Tibetan Plateau: *Geology*, 39 (4), 359-362. Doi:
570 10.1130/g31356.1.
- 571 Lease, R. O., Burbank, D. W., Zhang, H., Liu, J., & Yuan, D. (2012), Cenozoic shortening budget for the northeastern
572 edge of the Tibetan Plateau: Is lower crustal flow necessary?: *Tectonics*, 31 (3). Doi: 10.1029/2011TC003066.
- 573 Li, B., Chen, X., Zuza, A. V., Hu, D., Ding, W., Huang, P., & Xu, S. (2019), Cenozoic cooling history of the North
574 Qilian Shan, northern Tibetan Plateau, and the initiation of the Haiyuan fault: Constraints from apatite- and
575 zircon-fission track thermochronology: *Tectonophysics*, 751 (109-124. Doi: 10.1016/j.tecto.2018.12.005.
- 576 Li, B., Feng, Q., Wang, X., Li, Z., Wang, F., Zhao, C., Yu, T., & Chen, W. (2023), Formation of the upper reaches of
577 the Yellow River: Provenance evidence from the strata of the Yellow River sedimentary basin: *Global and*
578 *Planetary Change*, 229 (104224. Doi: 10.1016/j.gloplacha.2023.104224.
- 579 Li, B., Wang, Y., Zuza, A. V., Chen, X., Shao, Z., Wang, Z.-Z., Sun, Y., & Wu, C. (2022), Cenozoic deformation in the
580 eastern domain of the North Qaidam thrust belt, northern Tibetan Plateau: *GSA Bulletin*, 135 (1-2), 331-350. Doi:
581 10.1130/b36215.1.
- 582 Li, G., Pettke, T., & Chen, J. (2011), Increasing Nd isotopic ratio of Asian dust indicates progressive uplift of the north

- 583 Tibetan Plateau since the middle Miocene: *Geology*, 39 (3), 199-202. Doi: 10.1130/g31734.1.
- 584 Li, J., Fang, X., Song, C., Pan, B., Ma, Y., & Yan, M. (2014a), Late Miocene–Quaternary rapid stepwise uplift of the
585 NE Tibetan Plateau and its effects on climatic and environmental changes: *Quaternary Research*, 81 (3), 400-
586 423. Doi: 10.1016/j.yqres.2014.01.002.
- 587 Li, L., & Garzione, C. N. (2023), Upward and outward growth of north-central Tibet: Mechanisms that build high-
588 elevation, low-relief plateaus: *Science Advances*, 9 (27), eadh3058. Doi: 10.1126/sciadv.adh3058.
- 589 Li, Y., Li, D., Liu, G., Harbor, J., Caffee, M., & Stroeven, A. P. (2014b), Patterns of landscape evolution on the central
590 and northern Tibetan Plateau investigated using in-situ produced ^{10}Be concentrations from river sediments:
591 *Earth and Planetary Science Letters*, 398 (77-89. Doi: 10.1016/j.epsl.2014.04.045.
- 592 Liang, H. Y., Feng, Z. P., Pei, B., Li, Y., & Yang, X. T. (2018), Demographic expansion of two *Tamarix* species along
593 the Yellow River caused by geological events and climate change in the Pleistocene: *Scientific Reports*, 8 (1), 60.
594 Doi: 10.1038/s41598-017-19034-x.
- 595 Lin, A., Yang, Z., Sun, Z., & Yang, T. (2001), How and when did the Yellow River develop its square bend?: *Geology*,
596 9 (10), 951–954. Doi: 10.1130/0091-7613(2001)029<0951:HAWDTY>2.0.CO;2.
- 597 Liu, P. (2015), Spatio-temporal evolution of Northeastern Tibetan Plateau: integrated provenance study of the Guide,
598 Lanzhou and Wushan-Tianshui basins [Doctor: Lanzhou University].
- 599 Lu, H., Fu, B., Shi, P., Ma, Y., & Li, H. (2016), Constraints on the uplift mechanism of northern Tibet: *Earth and*
600 *Planetary Science Letters*, 453 (108-118. Doi: 10.1016/j.epsl.2016.08.010.
- 601 Märki, L., Lupker, M., France-Lanord, C., Lavé, J., Gallen, S., Gajurel, A. P., Haghipour, N., Leuenberger-West, F., &
602 Eglinton, T. (2021), An unshakable carbon budget for the Himalaya: *Nature Geoscience*, 14 (10), 745-750. Doi:
603 10.1038/s41561-021-00815-z.
- 604 Medvedev, S., Beaumont, C., Law, R. D., Searle, M. P., & Godin, L. (2006), Growth of continental plateaus by channel
605 injection: models designed to address constraints and thermomechanical consistency, Channel Flow, Ductile
606 Extrusion and Exhumation in Continental Collision Zones, Volume 268, Geological Society of London, p. 147-
607 164.
- 608 Miao, Y., Fang, X., Sun, J., Xiao, W., Yang, Y., Wang, X., Farnsworth, A., Huang, K., Ren, Y., Wu, F., Qiao, Q., Zhang,
609 W., Meng, Q., Yan, X., Zheng, Z., Song, C., & Utescher, T. (2022), A new biologic paleoaltimetry indicating Late
610 Miocene rapid uplift of northern Tibet Plateau: *Science*, 378 (6624), 1074-1079. Doi:
611 doi:10.1126/science.abo2475.
- 612 Nie, J., Stevens, T., Rittner, M., Stockli, D., Garzanti, E., Limonta, M., Bird, A., Ando, S., Vermesch, P., Saylor, J.,
613 Lu, H., Breecker, D., Hu, X., Liu, S., Resentini, A., Vezzoli, G., Peng, W., Carter, A., Ji, S., & Pan, B. (2015),
614 Loess Plateau storage of Northeastern Tibetan Plateau-derived Yellow River sediment: *Nat Commun*, 6 (8511).
615 Doi: 10.1038/ncomms9511.
- 616 Pan, B., Su, H., Hu, Z., Hu, X., Gao, H., Li, J., & Kirby, E. (2009), Evaluating the role of climate and tectonics during
617 non-steady incision of the Yellow River: evidence from a 1.24Ma terrace record near Lanzhou, China:
618 *Quaternary Science Reviews*, 28 (27), 3281-3290. Doi: 10.1016/j.quascirev.2009.09.003.
- 619 Perron, J. T., & Royden, L. (2013), An integral approach to bedrock river profile analysis: *Earth Surface Processes*

- 620 *and Landforms*, 38 (6), 570-576. Doi: 10.1002/esp.3302.
- 621 Polissar, P. J., Freeman, K. H., Rowley, D. B., McInerney, F. A., & Currie, B. S. (2009), Paleoaltimetry of the Tibetan
622 Plateau from D/H ratios of lipid biomarkers: *Earth and Planetary Science Letters*, 287 (1-2), 64-76. Doi:
623 10.1016/j.epsl.2009.07.037.
- 624 Pritchard, D., Roberts, G. G., White, N. J., & Richardson, C. N. (2009), Uplift histories from river profiles:
625 *Geophysical Research Letters*, 36 (24). Doi: 10.1029/2009gl040928.
- 626 Racano, S., Schildgen, T. F., Cosentino, D., & Miller, S. R. (2021), Temporal and Spatial Variations in Rock Uplift
627 From River-Profile Inversions at the Central Anatolian Plateau Southern Margin: *Journal of Geophysical
628 Research: Earth Surface*, 126 (8), e2020JF006027. Doi: 10.1029/2020JF006027.
- 629 Reusser, L. J., Bierman, P. R., Pavich, M. J., Zen, E.-a., Larsen, J., & Finkel, R. (2004), Rapid Late Pleistocene Incision
630 of Atlantic Passive-Margin River Gorges: *Science*, 305 (5683), 499-502. Doi: doi:10.1126/science.1097780.
- 631 Roberts, G. G., White, N. J., Martin-Brandis, G. L., & Crosby, A. G. (2012), An uplift history of the Colorado Plateau
632 and its surroundings from inverse modeling of longitudinal river profiles: *Tectonics*, 31 (4), n/a-n/a. Doi:
633 10.1029/2012tc003107.
- 634 Rowley, D. B., & Currie, B. S. (2006), Palaeo-altimetry of the late Eocene to Miocene Lunpola basin, central Tibet:
635 *Nature*, 439 (7077), 677-681. Doi: 10.1038/nature04506.
- 636 Royden, L. H., Burchfiel, B. C., King, R. W., Wang, E., Chen, Z., Shen, F., & Liu, Y. (1997), Surface Deformation
637 and Lower Crustal Flow in Eastern Tibet: *Science*, 276 (5313), 788-790. Doi: 10.1126/science.276.5313.788.
- 638 Royden, L. H., Burchfiel, B. C., & van der Hilst, R. D. (2008), The geological evolution of the Tibetan Plateau: *Science*,
639 321 (5892), 1054-1058. Doi: 10.1126/science.1155371.
- 640 Shen, X., Braun, J., & Yuan, X. (2022), Southeastern margin of the Tibetan Plateau stopped expanding in the late
641 Miocene: *Earth and Planetary Science Letters*, 583 (117446). Doi: 10.1016/j.epsl.2022.117446.
- 642 Staisch, L. M., Niemi, N. A., Clark, M. K., & Chang, H. (2016), Eocene to late Oligocene history of crustal shortening
643 within the Hoh Xil Basin and implications for the uplift history of the northern Tibetan Plateau: *Tectonics*, 35 (4),
644 862-895. Doi: 10.1002/2015tc003972.
- 645 Su, Q., Wang, X., Yuan, D., Xie, H., Li, H., & Huang, X. (2023), Fluvial entrenchment of the Gonghe Basin and
646 integration of the upper Yellow River - Evidence from the cosmogenically dated geomorphic surfaces:
647 *Geomorphology*, 429 (Doi: 10.1016/j.geomorph.2023.108654).
- 648 Su, T., Farnsworth, A., Spicer, R. A., Huang, J., Wu, F.-X., Liu, J., Li, S.-F., Xing, Y.-W., Huang, Y.-J., Deng, W.-Y.-
649 D., Tang, H., Xu, C.-L., Zhao, F., Srivastava, G., Valdes, P. J., Deng, T., & Zhou, Z.-K. (2019), No high Tibetan
650 Plateau until the Neogene: *Science Advances*, 5 (3), eaav2189. Doi: 10.1126/sciadv.aav2189.
- 651 Sun, B., Wang, Y. F., Li, C. S., Yang, J., Li, J. F., Li, Y. L., Deng, T., Wang, S. Q., Zhao, M., Spicer, R. A., Ferguson,
652 D. K., & Mehrotra, R. C. (2015), Early Miocene elevation in northern Tibet estimated by palaeobotanical
653 evidence: *Scientific Reports*, 5 (10379). Doi: 10.1038/srep10379.
- 654 Tapponnier, P., Meyer, B., Avouac, J. P., Peltzer, G., Gaudemer, Y., Guo, S., Xiang, H., Yin, K., Chen, Z., Cai, S., &
655 Dai, H. (1990), Active thrusting and folding in the Qilian Shan, and decoupling between upper crust and mantle
656 in northeastern Tibet: *Earth and Planetary Science Letters*, 97 (3), 382-403. Doi: 10.1016/0012-821X(90)90053-

- 657 Z.
- 658 Tapponnier, P., Zhiqin, X., Roger, F., Meyer, B., Arnaud, N., Wittlinger, G., & Jingsui, Y. (2001), Oblique Stepwise
659 Rise and Growth of the Tibet Plateau: *Science*, 294 (5547), 1671-1677. Doi: 10.1126/science.105978.
- 660 Unsworth, M., Wei, W., Jones, A., Li, S., Bedrosian, P., Booker, J., Jin, S., Deng, M., & Tan, H. (2004), Crustal and
661 upper mantle structure of northern Tibet imaged with magnetotelluric data: *Journal of Geophysical Research-Solid Earth*, 109 (Doi: 10.1029/2002JB002305).
- 663 Wang, C., Dai, J., Zhao, X., Li, Y., Graham, S. A., He, D., Ran, B., & Meng, J. (2014), Outward-growth of the Tibetan
664 Plateau during the Cenozoic: A review: *Tectonophysics*, 621 (1-43. Doi: 10.1016/j.tecto.2014.01.036.
- 665 Wang, W., Zhang, P., Garzione, C. N., Liu, C., Zhang, Z., Pang, J., Wang, Y., Zheng, D., Zheng, W., & Zhang, H.
666 (2022), Pulsed rise and growth of the Tibetan Plateau to its northern margin since ca. 30 Ma: *Proc Natl Acad Sci
667 USA*, 119 (8). Doi: 10.1073/pnas.2120364119.
- 668 Wang, W., Zheng, D., Li, C., Wang, Y., Zhang, Z., Pang, J., Wang, Y., Yu, J., Wang, Y., Zheng, W., Zhang, H., & Zhang,
669 P. (2020), Cenozoic Exhumation of the Qilian Shan in the Northeastern Tibetan Plateau: Evidence From Low-
670 Temperature Thermochronology: *Tectonics*, 39 (4). Doi: 10.1029/2019tc005705.
- 671 Wang, W., Zheng, W., Zhang, P., Li, Q., Kirby, E., Yuan, D., Zheng, D., Liu, C., Wang, Z., Zhang, H., & Pang, J.
672 (2017), Expansion of the Tibetan Plateau during the Neogene: *Nature Communications*, 8 (15887. Doi:
673 10.1038/ncomms15887.
- 674 Wang, X., Vandenberghe, J., Yi, S., Van Balen, R., & Lu, H. (2015), Climate-dependent fluvial architecture and
675 processes on a suborbital timescale in areas of rapid tectonic uplift: An example from the NE Tibetan Plateau:
676 *Global and Planetary Change*, 133 (318-329. Doi: 10.1016/j.gloplacha.2015.09.009.
- 677 Whipple, K. X., & Tucker, G. E. (1999), Dynamics of the stream-power river incision model: Implications for height
678 limits of mountain ranges, landscape response timescales, and research needs: *Journal of Geophysical Research: Solid Earth*, 104 (B8), 17661-17674. Doi: 10.1029/1999jb900120.
- 680 Wolf, S. G., Huismans, R. S., Braun, J., & Yuan, X. (2022), Topography of mountain belts controlled by rheology and
681 surface processes: *Nature*, 606 (7914), 516-521. Doi: 10.1038/s41586-022-04700-6.
- 682 Yan, M., VanderVoo, R., Fang, X.-m., Parés, J. M., & Rea, D. K. (2006), Paleomagnetic evidence for a mid-Miocene
683 clockwise rotation of about 25° of the Guide Basin area in NE Tibet: *Earth and Planetary Science Letters*, 241
684 (1-2), 234-247. Doi: 10.1016/j.epsl.2005.10.013.
- 685 Yin, A., Dang, Y.-Q., Zhang, M., Chen, X.-H., & McRivette, M. W. (2008), Cenozoic tectonic evolution of the Qaidam
686 basin and its surrounding regions (Part 3): Structural geology, sedimentation, and regional tectonic reconstruction:
687 *GSA Bulletin*, 120 (7-8), 847-876. Doi: 10.1130/b26232.1.
- 688 Yin, A., & Harrison, T. M. (2000), Geologic Evolution of the Himalayan-Tibetan Orogen: *Annual Review of Earth
689 and Planetary Sciences*, 28 (1), 211-280. Doi: 10.1146/annurev.earth.28.1.211.
- 690 Yu, J., Zheng, D., Wang, W., Pang, J., Li, C., Wang, Y., Hao, Y., Zhang, H., & Zhang, P. (2023), Cenozoic tectonic
691 development in the northeastern Tibetan Plateau: Evidence from thermochronological and sedimentological
692 records: *Global and Planetary Change*, 224 (104098. Doi: 10.1016/j.gloplacha.2023.104098.
- 693 Yuan, D. Y., Champagnac, J. D., Ge, W. P., Molnar, P., Zhang, P. Z., Zheng, W. J., Zhang, H. P., & Liu, X. W. (2011),

- 694 Late Quaternary right-lateral slip rates of faults adjacent to the lake Qinghai, northeastern margin of the Tibetan
695 Plateau: *Geological Society of America Bulletin*, 123 (9-10), 2016-2030. Doi: 10.1130/b30315.1.
- 696 Yuan, D. Y., Ge, W. P., Chen, Z. W., Li, C. Y., Wang, Z. C., Zhang, H. P., Zhang, P. Z., Zheng, D. W., Zheng, W. J.,
697 Craddock, W. H., Dayem, K. E., Duvall, A. R., Hough, B. G., Lease, R. O., Champagnac, J. D., Burbank, D. W.,
698 Clark, M. K., Farley, K. A., Garzione, C. N., Kirby, E., Molnar, P., & Roe, G. H. (2013), The growth of
699 northeastern Tibet and its relevance to large-scale continental geodynamics: A review of recent studies: *Tectonics*,
700 32 (5), 1358-1370. Doi: 10.1002/tect.20081.
- 701 Yuan, X. P., Braun, J., Guerit, L., Rouby, D., & Cordonnier, G. (2019), A New Efficient Method to Solve the Stream
702 Power Law Model Taking Into Account Sediment Deposition: *Journal of Geophysical Research: Earth Surface*,
703 124 (6), 1346-1365. Doi: 10.1029/2018jf004867.
- 704 Yuan, X. P., Huppert, K. L., Braun, J., Shen, X., Liu-Zeng, J., Guerit, L., Wolf, S. G., Zhang, J. F., & Jolivet, M. (2021),
705 Propagating uplift controls on high-elevation, low-relief landscape formation in the southeast Tibetan Plateau:
706 *Geology*, 50 (1), 60-65. Doi: 10.1130/g49022.1.
- 707 Yuan, X. P., Jiao, R., Dupont-Nivet, G., & Shen, X. (2022), Southeastern Tibetan Plateau Growth Revealed by Inverse
708 Analysis of Landscape Evolution Model: *Geophysical Research Letters*, 49 (10). Doi: 10.1029/2021gl097623.
- 709 Yuan, X. P., Jiao, R., Liu-Zeng, J., Dupont-Nivet, G., Wolf, S. G., & Shen, X. (2023), Downstream propagation of
710 fluvial erosion in Eastern Tibet: *Earth and Planetary Science Letters*, 605 (Doi: 10.1016/j.epsl.2023.118017.
- 711 Zhang, H., Kirby, E., Pitlick, J., Anderson, R. S., & Zhang, P. (2017a), Characterizing the transient geomorphic
712 response to base-level fall in the northeastern Tibetan Plateau: *Journal of Geophysical Research: Earth Surface*,
713 122 (2), 546-572. Doi: 10.1002/2015JF003715.
- 714 Zhang, H., Zhang, P., Champagnac, J. D., Molnar, P., Anderson, R. S., Kirby, E., Craddock, W. H., & Liu, S. (2014),
715 Pleistocene drainage reorganization driven by the isostatic response to deep incision into the northeastern Tibetan
716 Plateau: *Geology*, 42 (4), 303-306. Doi: 10.1130/g35115.1.
- 717 Zhang, P., Burchfiel, B. C., Molnar, P., Zhang, W., Jiao, D., Deng, Q., Wang, Y., Royden, L., & Song, F. (1991),
718 Amount and style of Late Cenozoic Deformation in the Liupan Shan Area, Ningxia Autonomous Region, China:
719 *Tectonics*, 10 (6), 1111-1129. Doi: 10.1029/90TC02686.
- 720 Zhang, W., Zhang, T., Song, C., Erwin, A., Mao, Z., Yahui, F., Yin, L., Qingquan, M., Rongsheng, Y., Dawen, Z.,
721 Bingshuai, L., & Jiao, L. (2017b), Termination of fluvial-alluvial sedimentation in the Xining Basin, NE Tibetan
722 Plateau, and its subsequent geomorphic evolution: *Geomorphology*, 297 (86-99). Doi:
723 10.1016/j.geomorph.2017.09.008.
- 724 Zhang, Y., Zhang, H., Ma, Z., Wang, Y., & Zhao, X. (2023), Inversion of Late Miocene uplift history from the transient
725 Daxia River landscape, NE Tibetan Plateau: *Journal of the Geological Society*, 180 (6). Doi: 10.1144/jgs2023-
726 030.
- 727 Zhao, Y., Fan, N., Nie, J., Abell, J. T., An, Y., Jin, Z., Wang, C., Zhang, J., Liu, X., & Nie, R. (2023), From Desiccation
728 to Re-Integration of the Yellow River Since the Last Glaciation: *Geophysical Research Letters*, 50 (15),
729 e2023GL103632. Doi: 10.1029/2023GL103632.
- 730 Zheng, D., Zhang, P.-Z., Wan, J., Yuan, D., Li, C., Yin, G., Zhang, G., Wang, Z., Min, W., & Chen, J. (2006), Rapid

- 731 exhumation at ~8 Ma on the Liupan Shan thrust fault from apatite fission-track thermochronology: Implications
732 for growth of the northeastern Tibetan Plateau margin: *Earth and Planetary Science Letters*, 248 (1-2), 198-208.
733 Doi: 10.1016/j.epsl.2006.05.023.
- 734 Zhuang, G., Brandon, M. T., Pagani, M., & Krishnan, S. (2014), Leaf wax stable isotopes from Northern Tibetan
735 Plateau: Implications for uplift and climate since 15 Ma: *Earth and Planetary Science Letters*, 390 (186-198. Doi:
736 10.1016/j.epsl.2014.01.003.
- 737 Zuza, A. V., Cheng, X., & Yin, A. (2016), Testing models of Tibetan Plateau formation with Cenozoic shortening
738 estimates across the Qilian Shan–Nan Shan thrust belt: *Geosphere*, 12 (2), 501-532. Doi: 10.1130/ges01254.1.